

Contrastive Geometric Learning Unlocks Unified Structure- and Ligand-Based Drug Design

Lisa Schneckenreiter¹ Sohvi Luukkonen¹ Lukas Friedrich² Daniel Kuhn² Günter Klambauer^{1,3}

Abstract

Structure-based and ligand-based computational drug design have traditionally relied on disjoint data sources and modeling assumptions, limiting their joint use at scale. In this work, we introduce **Contrastive Geometric Learning for Unified Computational Drug Design** (ConGLUDe), a single contrastive geometric model that unifies structure- and ligand-based training. ConGLUDe couples a geometric protein encoder that produces whole-protein representations and implicit embeddings of predicted binding sites with a fast ligand encoder, removing the need for pre-defined pockets. By aligning ligands with both global protein representations and multiple candidate binding sites through contrastive learning, ConGLUDe supports ligand-conditioned pocket prediction in addition to virtual screening and target fishing, while being trained jointly on protein–ligand complexes and large-scale bioactivity data. Across diverse benchmarks, ConGLUDe achieves state-of-the-art zero-shot virtual screening performance in settings where no binding pocket information is provided as input, substantially outperforms existing methods on a challenging target fishing task, and demonstrates competitive ligand-conditioned pocket selection. These results highlight the advantages of unified structure–ligand training and position ConGLUDe as a step toward general-purpose foundation models for drug discovery.

1. Introduction

Protein–ligand interactions play a crucial role in drug discovery. Most therapeutics are small molecules, referred

¹ELLIS Unit Linz, LIT AI Lab, Institute for Machine Learning, Johannes Kepler University Linz, Austria ²Medicinal Chemistry & Drug Design, Merck Healthcare KGaA, Darmstadt, Germany

³Clinical Research Institute for Medical Artificial Intelligence, Johannes Kepler University, Linz, Austria. Correspondence to: Lisa Schneckenreiter <schneckenreiter@ml.jku.at>.

Preprint. January 15, 2026.

to as ligands, that bind to disease-associated protein targets to modulate their function (Kinch et al., 2024). Understanding protein–ligand interactions (PLIs) through modeling atomic interactions at binding sites or more general ligand bioactivity measures enables rational drug design (Gohlke et al., 2000; Du et al., 2016). Computational methods for predicting and analyzing these interactions have been used for decades, and recent advances in artificial intelligence (AI) and machine learning (ML) have greatly expanded their accuracy and applicability. These approaches are commonly grouped into two paradigms: structure-based drug design (SBDD) and ligand-based drug design (LBDD) (Macalino et al., 2015; Vemula et al., 2023), with disjoint data sources and modalities.

SBDD relies on structural data describing the 3D conformations of ligands bound to protein binding sites. Generally, this information is derived from experimentally resolved protein–ligand complexes, obtained using, e.g., X-ray crystallography or NMR spectroscopy (Mutharasappan et al., 2020), a technically demanding process that has historically limited the application of SBDD to only a fraction of known proteins. Experimental structures are systematically archived in the Protein Data Bank (PDB) (Berman et al., 2000), which contains $\sim 245k$ entries¹. This provides a valuable resource for SBDD, although only a fraction of entries contain biologically relevant ligands, and the total number of available ligands is limited.

In computational SBDD, the binding potential of candidate molecules to a specific pocket is typically assessed using methods such as docking (Kuntz et al., 1982; Fan et al., 2019), molecular dynamics (De Vivo et al., 2016), or free energy perturbation (Beveridge & Dicapua, 1989; Cournia et al., 2021). More recently, AI innovations have enabled the holistic prediction of protein–ligand complexes – without explicit binding pocket information as input – either with AI-based blind docking methods (Stärk et al., 2022; Corso et al., 2023; Pei et al., 2024), or foundation models for molecular structure prediction of biological complexes (Abramson et al., 2024; Wohlwend et al., 2024; Discovery et al., 2024). However, by modeling exact binding positions,

¹From <https://www.rcsb.org/stats/growth/growth-released-structures>. Accessed on 15/12/2025.

these methods are inherently computationally demanding, making them unsuitable for large-scale virtual screening.

LBDD uses bioactivity data from large-scale biochemical assays. Rather than modeling explicit binding geometries, LBDD learns ligand activity directly from experimental assay outcomes and therefore does not depend on knowledge of the ligand’s binding conformation within the protein target (Merz Jr et al., 2010). This paradigm is supported by large public resources such as PubChem, which contains approximately 300M bioactivity measurements (Kim et al., 2024), and ChEMBL, which provides curated bioactivity data across thousands of targets (Gaulton et al., 2011).

This wealth of data has made ML central to LBDD since the early 1990s (Hansch et al., 1962; Muratov et al., 2020), initially through classical quantitative structure-activity relationship (QSAR) models such as support vector machines (Burbidge et al., 2001) and random forests (Svetnik et al., 2003), and more recently through gradient boosting (Babajide Mustapha & Saeed, 2016; Sheridan et al., 2016) and deep learning approaches (Lenselink et al., 2017; Mayr et al., 2018; Yang et al., 2019). Historically, ML-based LBDD was limited to protein targets with sufficient experimental data to train target-specific models. Recent few-shot and zero-shot learning methods have extended activity prediction to scarce-data regimes (Vella & Ebejer, 2022; Schimunek et al., 2023; Seidl et al., 2023). While traditional LBDD relies solely on ligand information, proteochemometrics augments these models with protein representations, such as sequence-derived descriptors or learned embeddings, enabling generalization to unseen targets (Lapinsh et al., 2001; Öztürk et al., 2018; Bongers et al., 2019; Svensson et al., 2024). With the advent of AlphaFold (Jumper et al., 2021), structural encoding of target proteins without available PDB entries has also become possible, further expanding the scope of ligand-based prediction.

Recently, contrastive learning has emerged as a powerful paradigm for modeling PLIs. These models embed protein and ligand representations in a shared latent space, where interactions are inferred via representational similarity, yielding substantial computational efficiency that enables genome-wide screens of large-scale compound libraries (Jia et al., 2026). When trained on structure-based data, they typically rely on explicitly encoding predefined binding pockets, thereby restricting their applicability to targets with known binding sites (Gao et al., 2024; Han et al., 2025; Feng et al., 2025; Wang et al., 2025; He et al., 2025). Conversely, contrastive models trained on ligand-based data use sequence- or structure-level encodings of entire proteins, allowing broader applicability but without enabling pocket-specific predictions (Singh et al., 2023; McNutt et al., 2024).

Combining both data types could yield more informative

protein and ligand representations. Previous attempts at unifying structure- and ligand-based data augment PDB complexes with ligand-based data either by assigning active ligands to known binding pockets – implicitly assuming the correct binding site (Gao et al., 2024; Feng et al., 2025; Wang et al., 2025) –, or by (blind) docking, which is computationally expensive and introduces pose uncertainty (Francœur et al., 2020; Brocidiacomo et al., 2024; Liu et al., 2024). Other approaches use the two data types to supervise different components of the model, such as a structure-prediction module with a separate affinity-prediction head (Passaro et al., 2025), or distinct encoders for protein sequences derived from ligand-based data and predefined binding pockets from structure-based data (He et al., 2025). Yet, no prior method fully integrates structure- and ligand-based training in a way that enables pocket-level predictions without relying on pre-defined pockets as input.

Contrastive geometric learning unlocks seamless integration of structure- and ligand-based data. We introduce *Contrastive Geometric Learning for Unified Computational Drug Design* (ConGLUDe), a method that combines a geometric protein encoder – providing whole-protein representations and implicit embeddings of predicted binding sites, thus eliminating the need for pre-defined pockets – with a fast, efficient ligand encoder via contrastive learning. Integrating pocket prediction capabilities into the protein encoder enables learning from both structure- and ligand-based data without losing pocket-specific information (Figure 1). The extension of the well-established CLIP-style

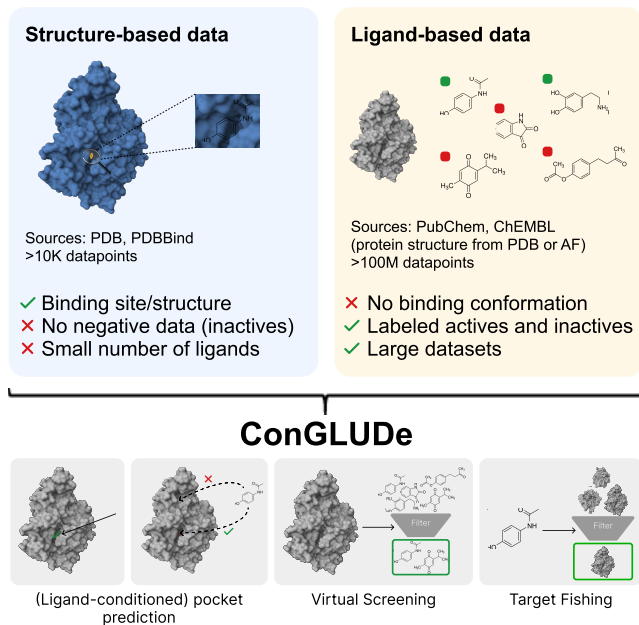


Figure 1. Joint training of ConGLUDe on structure- and ligand-based data enables (ligand-conditioned) pocket prediction, virtual screening and target fishing.

contrastive loss to a third axis – along different predicted binding sites on a protein – allows for the introduction of the novel ligand-conditioned pocket prediction task, which focuses on the identification of a specific ligand’s binding site without resorting to inefficient blind docking or co-folding. With this unified approach, ConGLUDe excels across diverse drug discovery applications, achieving state-of-the-art virtual screening – in settings where no binding pocket information is provided as input – and binding site prediction, performing competitively with slower docking methods on ligand-conditioned pocket prediction, and substantially outperforming all baselines on a novel target fishing dataset.

2. Background and Preliminaries

2.1. Notation and Definitions

Protein–ligand interaction data point. A PLI data point is defined as a triplet $(\mathcal{G}, \mathcal{M}, y)$, where \mathcal{G} denotes a protein, \mathcal{M} a ligand (typically a small molecule), and y a binary or real-valued label. In structure-based datasets, PLIs data points are derived from experimentally resolved 3D structures of protein–ligand complexes. Protein–ligand pairs with observed co-crystal structures are labeled as positives ($y = 1$), while all other combinations are treated as negatives ($y = 0$). In contrast, ligand-based datasets provide activity measurements for a large set of small molecules tested against a given target protein, typically obtained through biological assays. Labels may be binary (active: $y = 1$, inactive: $y = 0$) or continuous affinity values ($y \in \mathbb{R}$), such as IC_{50} or K_d .

Protein and ligand representations. We represent proteins as geometric graphs \mathcal{G} , where each node corresponds to an amino acid residue. Each node is assigned a 3D coordinate (specifically, the position of the C_α atom) and a feature vector encoding residue-specific properties, extracted using ESM-2 (Lin et al., 2023). Edges connect each node to a maximum of 10 nearest neighbors within a 10 Å radius. Ligands are represented as fixed-length vectors constructed by concatenating Morgan fingerprints (Morgan, 1965) with RDKit chemical descriptors (Landrum & contributors, 2006).

Definition of binding sites. Structure-based datasets enable direct annotation of protein binding sites – the regions where ligands interact with the protein. Here, we define a binding site for a given ligand as the geometric center $\mathbf{z} \in \mathbb{R}^3$ of all protein residues that lie within a 4 Å radius of any ligand atom.

An overview of all notation used in this work is provided in Appendix A.

2.2. Binding Pocket Prediction Using VN-EGNN

When experimental binding site annotations are unavailable, accurately identifying binding pockets becomes a critical step in SBDD. Sestak et al. (2025) proposed an approach based on an equivariant graph neural network with virtual nodes (VN-EGNN) to address this task. In this framework, the protein is represented as a geometric graph (as described above), augmented with a small set of virtual nodes. Each virtual node is initialized with a coordinate on a sphere around the protein and a feature vector given by the mean of all protein residue embeddings. Virtual nodes are connected to every protein residue, enabling the network to integrate both local and global structural information. VN-EGNN employs a three-step heterogeneous message-passing scheme between protein and virtual nodes, detailed in Appendix B.1. The model is trained with a combination of three objective functions (see Appendix B.2) to predict the 3D coordinates of potential binding pockets, denoted by the final virtual node positions $\mathbf{z}'_1, \dots, \mathbf{z}'_N \in \mathbb{R}^3$, where N is the number of virtual nodes. In addition to predicting binding site centers, the model outputs pocket-level feature representations $\mathbf{b}'_1, \dots, \mathbf{b}'_N \in \mathbb{R}^E$ from the final layer. These embeddings are used to assign confidence scores to predicted pockets and can facilitate downstream tasks such as pocket ranking or contrastive learning.

2.3. Virtual Screening Using Contrastive Learning

Contrastive learning provides a general framework for modeling protein–ligand interactions by embedding proteins and ligands into a shared latent space, in which interaction likelihood is assessed via embedding similarity (Singh et al., 2023; Gao et al., 2024; Han et al., 2025; Wang et al., 2024; McNutt et al., 2024; Gil-Sorribes et al., 2025). Most contrastive models in this setting follow a common architectural pattern composed of three core components:

- a *molecule encoder*, which projects ligand representations into the shared latent space,
- a *protein and pocket encoder*, which maps sequence- or structure-based representations of the target protein or binding site into the same space, and
- a *contrastive loss function*, that pulls interacting protein–ligand pairs together in the embedding space while pushing non-interacting pairs apart.

A defining property of this framework is its separation of representation learning from interaction scoring: once embeddings are computed, virtual screening reduces to efficient similarity evaluations between protein and ligand representations, enabling scalable large-scale screening without explicit docking.

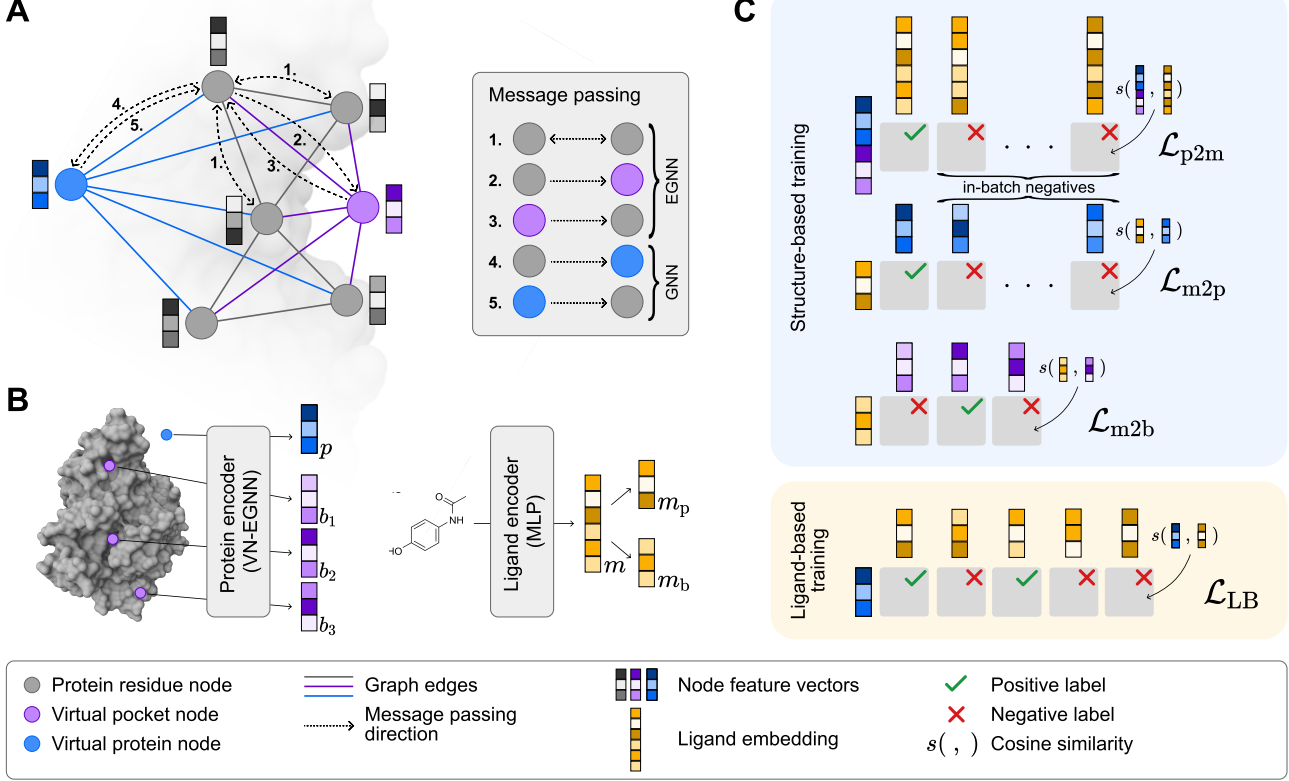


Figure 2. ConGLUDe architecture and training procedure. **A:** Message-passing scheme of ConGLUDe's protein encoder based on VN-EGNN: 1. message exchange between residue nodes, 2. residue nodes to virtual pocket nodes, 3. pocket nodes to residue nodes, 4. residue nodes to virtual protein node, 5. virtual protein node to residue nodes. **B:** The protein encoder supplies a representation of the whole protein \mathbf{p} , and of each detected pocket \mathbf{b}_k . The ligand encoder encodes each small molecule into a protein matching representation \mathbf{m}_p and a pocket-matching representation \mathbf{m}_b . **C:** Contrastive loss functions used in our approach. Structure-based losses include \mathcal{L}_{p2m} : InfoNCE between a concatenated protein-pocket representation and all ligand representations from the batch, \mathcal{L}_{m2p} : InfoNCE between a ligand and all protein representations in the batch, and \mathcal{L}_{m2b} : InfoNCE between a ligand and all pocket representations from the corresponding protein. The NCE loss between a protein and annotated ligand representations (\mathcal{L}_{LB}) is used on ligand-based data.

3. Contrastive Geometric Learning for Unified Drug Design (ConGLUDe)

ConGLUDe is a contrastive model that employs a geometric *protein encoder* based on a modified VN-EGNN (Sestak et al., 2025) architecture, which predicts candidate binding site locations $\hat{\mathbf{z}}_1, \dots, \hat{\mathbf{z}}_K \in \mathbb{R}^3$ together with corresponding representations $\mathbf{b}_1, \dots, \mathbf{b}_K \in \mathbb{R}^D$ as well as a global protein embedding $\mathbf{p} \in \mathbb{R}^D$. A complementary *molecule encoder* maps ligands into representations $\mathbf{m} \in \mathbb{R}^{2D}$, aligned with the concatenated protein/pocket embeddings $[\mathbf{b}_i, \mathbf{p}]$.

ConGLUDe integrates structure- and ligand-based learning by alternating between (i) structure-based batches, where it learns to detect and characterize binding sites and pair them with their ligands, and (ii) ligand-based batches, where it leverages large-scale bioactivity measurements. Figure 2 provides an overview of the architecture and training procedure.

3.1. ConGLUDe Architecture

3.1.1. PROTEIN AND BINDING POCKET ENCODERS

We extend the original VN-EGNN formulation by introducing an additional non-geometric virtual node \mathcal{P} , which aggregates information from the entire protein but has no spatial coordinates. In addition to the three geometric message-passing steps of VN-EGNN (Appendix B.1), we add two non-geometric steps from residue nodes to the protein node ($\mathcal{R} \rightarrow \mathcal{P}$) and vice versa. ($\mathcal{P} \rightarrow \mathcal{R}$):

Message passing step 4 ($\mathcal{R} \rightarrow \mathcal{P}$):

$$\mu_j^{(\mathcal{R}\mathcal{P})} = \phi_{e(\mathcal{R}\mathcal{P})}(\mathbf{p}, \mathbf{h}_j) \quad (1)$$

$$\boldsymbol{\mu}^{(\mathcal{R}\mathcal{P})} = \frac{1}{S} \sum_{j=1}^S \mu_j^{(\mathcal{R}\mathcal{P})} \quad (2)$$

$$\mathbf{p} = \mathbf{p} + \phi_{h(\mathcal{R}\mathcal{P})}(\mathbf{p}, \boldsymbol{\mu}^{(\mathcal{R}\mathcal{P})}) \quad (3)$$

Message passing step 5 ($\mathcal{P} \rightarrow \mathcal{R}$):

$$\boldsymbol{\mu}_i^{(\mathcal{P}\mathcal{R})} = \phi_{e^{(\mathcal{P}\mathcal{R})}}(\boldsymbol{h}_i, \boldsymbol{p}) \quad (4)$$

$$\boldsymbol{h}_i = \boldsymbol{h}_i + \phi_{h^{(\mathcal{B}\mathcal{R})}}(\boldsymbol{h}_i, \boldsymbol{\mu}_i^{(\mathcal{P}\mathcal{R})}) \quad (5)$$

Here, $\boldsymbol{\mu}_j^{(\mathcal{R}\mathcal{P})}$ denotes the messages sent from residue node j to the protein node, while $\boldsymbol{\mu}_i^{(\mathcal{P}\mathcal{R})}$ denotes the reverse direction. The functions $\phi_{e^{(\mathcal{P}\mathcal{R})}}$, $\phi_{h^{(\mathcal{R}\mathcal{P})}}$, $\phi_{e^{(\mathcal{P}\mathcal{R})}}$ and $\phi_{h^{(\mathcal{B}\mathcal{R})}}$ are layer-specific multi-layer-perceptrons (MLPs) of the graph neural network (GNN). Our model uses 5 layers of VN-EGNN, but we omit the layer index in Eq. B.1–B.12 and Eq. 1–5 for clarity. Applying the structure encoder to a protein graph \mathcal{G} yields

$$\mathbf{X}', \mathbf{H}', \mathbf{Z}', \mathbf{B}', \mathbf{p}' = \text{VNEGNN}(\mathcal{G}), \quad (6)$$

where $\mathbf{X}' = (\mathbf{x}'_1, \dots, \mathbf{x}'_S) \in \mathbb{R}^{S \times 3}$ and $\mathbf{H}' = (\mathbf{h}'_1, \dots, \mathbf{h}'_S) \in \mathbb{R}^{S \times E}$ are the residue coordinates and features, $\mathbf{Z}' = (\mathbf{z}'_1, \dots, \mathbf{z}'_N) \in \mathbb{R}^{N \times 3}$ and $\mathbf{B}' = (\mathbf{b}'_1, \dots, \mathbf{b}'_N) \in \mathbb{R}^{N \times E}$ are the coordinates and feature representations of the virtual nodes representing binding pockets, and \mathbf{p}' is the global protein embedding from the protein virtual node.

To rank binding pocket predictions by confidence, we follow [Sestak et al. \(2025\)](#) and apply a two-layer MLP with scalar outputs to the pocket representations: $\mathbf{c}' = \text{MLP}(\mathbf{B}')$, $\mathbf{c}' \in \mathbb{R}^N$. Since multiple virtual nodes may converge to the same binding pocket, we cluster them based on their spatial coordinates using DBSCAN ([Ester et al., 1996](#)). For each cluster, we then compute the mean of the coordinates, feature vectors, and confidence values, yielding $\hat{\mathbf{Z}} \in \mathbb{R}^{K \times 3}$, $\hat{\mathbf{B}} \in \mathbb{R}^{K \times E}$, and $\hat{\mathbf{c}} \in \mathbb{R}^K$ with $K < N$. Finally, pocket- and protein-level representations are projected into the contrastive embedding space of dimension D via linear transformations: $\mathbf{B} = \text{Linear}(\hat{\mathbf{B}})$, $\mathbf{p} = \text{Linear}(\mathbf{p}')$.

3.1.2. LIGAND ENCODER

For the ligand encoder, we adopt a simple yet effective design motivated by prior work, which has shown that molecular fingerprints combined with MLPs often outperform more complex architectures such as GNNs for encoding small molecules ([Unterthiner et al., 2014](#); [Siemers et al., 2022](#); [Luukkonen et al., 2023](#); [Seidl et al., 2023](#); [Praski et al., 2025](#)). Specifically, a 2-layer MLP projects each molecule into a joint $2D$ -dimensional embedding $\mathbf{m} \in \mathbb{R}^{2D}$, which is then split into a protein-matching representation $\mathbf{m}_p \in \mathbb{R}^D$ and a pocket-matching representation $\mathbf{m}_b \in \mathbb{R}^D$:

$$\mathbf{m} = [\mathbf{m}_p, \mathbf{m}_b] = \text{MLP}(\mathcal{M}), \quad \mathbf{m} \in \mathbb{R}^{2D}. \quad (7)$$

This lightweight architecture enables simultaneous encoding of large batches of ligands, making it well-suited for high-throughput virtual screening across extensive compound libraries.

3.1.3. INFERENCE MODES

ConGLUDe supports multiple inference modes. In classical *virtual screening*, predictions are made by comparing the protein representation with the protein-specific component of the ligand embedding, $s(\mathbf{p}, \mathbf{m}_p)$, where $s(\cdot, \cdot)$ denotes the cosine similarity and higher similarity indicates a higher likelihood of binding. This formulation also applies to *target fishing*, where a ligand is tested across multiple proteins. For *binding site identification*, the VN-EGNN-based encoder directly outputs candidate pocket centers with confidence values. Predicted pockets can be ranked either ligand-independently by these confidence scores or in a ligand-conditioned manner by their similarity to the pocket-specific component of the ligand embedding, $s(\mathbf{b}_l, \mathbf{m}_b)$.

3.2. ConGLUDe Training

3.2.1. DATA

The ConGLUDe architecture enables training on a ligand-protein pairs from both structure-based and ligand-based databases. For each task, structure-based training data, a subset of PDBBind ([Wang et al., 2005](#)), are derived from the respective baseline methods. As ligand-based data we use the MERGED dataset curated by [McNutt et al. \(2024\)](#), which combines PubChem ([Kim et al., 2024](#)), BindingDB ([Gilson et al., 2015](#)), and ChEMBL ([Gaulton et al., 2011](#)) and remove all proteins with $>90\%$ sequence identity to any test set protein. For details on all datasets, see Appendix C.

3.2.2. TRAINING OBJECTIVE

The ConGLUDe objective is to minimize the loss on both structure-based and ligand-based data:

$$\mathcal{L} = \mathcal{L}_{\text{SB}} + \mathcal{L}_{\text{LB}}, \quad (8)$$

where \mathcal{L}_{SB} is the loss on structure-based training data and \mathcal{L}_{LB} is the loss on ligand-based training data, which are detailed further below. During training, each step samples a batch of either structure-based or ligand-based data at random, and the optimization objective is applied accordingly.

Training on structure-based data. For structure-based data, annotated protein binding sites provide supervision for binding site prediction. In this setting, the loss decomposes into a geometric term and a contrastive term:

$$\mathcal{L}_{\text{SB}} = \mathcal{L}_{\text{geometric}} + \mathcal{L}_{\text{contrastive}}. \quad (9)$$

The geometric component, $\mathcal{L}_{\text{geometric}}$, is equivalent to the objective function of VN-EGNN (see Appendix B.2).

Beyond the geometric objective, we leverage contrastive learning to align the representations of ligands with their corresponding proteins and predicted binding pockets. For a given protein-ligand complex, the ligand embedding \mathbf{m}^j

is encouraged to be close in representation space to the concatenated protein and pocket embeddings $[\mathbf{p}^j, \mathbf{b}_l^j]$, where \mathbf{b}_l^j is the predicted pocket closest to the ligand's true binding site center \mathbf{z} : $l = \operatorname{argmin}_{k=1, \dots, K} (\|\mathbf{z} - \hat{\mathbf{z}}_k\|)$.

This alignment is implemented using a three-way InfoNCE loss (Eq. A.1), similar to CLIP (Radford et al., 2021), aligning protein, pocket, and ligand embeddings along complementary axes. Along the first axis – “protein+pocket to molecule” – the concatenated protein and pocket representation, $[\mathbf{p}^j, \mathbf{b}_l^j]$, acts as the anchor, and the model is trained to associate it with its true ligand \mathbf{m}^j while treating other ligands in the batch as negatives:

$$\mathcal{L}_{\text{p2m}}^j = \text{InfoNCE}([\mathbf{p}^j, \mathbf{b}_l^j], \mathbf{m}^j, \{\mathbf{m}^i\}_{i=1}^J; \tau_{\text{p2m}}). \quad (10)$$

The second axis aligns the protein-matching component of the ligand embedding, \mathbf{m}_p^j , with the global protein representation \mathbf{p}^j , while contrasting it against other proteins in the mini-batch (“molecule to protein”):

$$\mathcal{L}_{\text{m2p}}^j = \text{InfoNCE}(\mathbf{m}_p^j, \mathbf{p}^j, \{\mathbf{p}^i\}_{i=1}^J; \tau_{\text{m2p}}). \quad (11)$$

Along the third axis – “molecule to binding site” – the pocket-matching component of the ligand embedding, \mathbf{m}_b^j , is aligned with the closest predicted binding pocket \mathbf{b}_l^j , contrasting it against the remaining predicted pockets on the same protein:

$$\mathcal{L}_{\text{m2b}}^j = \text{InfoNCE}(\mathbf{m}_b^j, \mathbf{b}_l^j, \{\mathbf{b}_k^j\}_{k=1}^K; \tau_{\text{m2b}}). \quad (12)$$

The temperature parameters are chosen as the inverse square root of the corresponding contrastive space dimension, i.e. $\tau_{\text{p2m}} = \frac{1}{\sqrt{2D}}$ and $\tau_{\text{m2p}} = \tau_{\text{m2b}} = \frac{1}{\sqrt{D}}$. The total contrastive loss is obtained by summing up the three loss axes and averaging over all samples in the batch:

$$\mathcal{L}_{\text{contrastive}} = \frac{1}{J} \sum_{j=1}^J \left(\mathcal{L}_{\text{p2m}}^j + \mathcal{L}_{\text{m2p}}^j + \mathcal{L}_{\text{m2b}}^j \right). \quad (13)$$

Alternative contrastive formulations, such as the CLOOB loss (Fürst et al., 2022; Sanchez-Fernandez et al., 2023), could also be used.

Training on ligand-based data. When training on ligand-based datasets, we leverage large collections of annotated active and inactive compounds for a given protein target. Since no structural information on the binding pocket is available in this setting, the VN-EGNN module cannot be meaningfully optimized and is therefore kept frozen during training. For each batch, active and inactive compounds are sampled at a ratio of 1:3, and the model is trained with a *sigmoid contrastive loss* (Gutmann & Hyvärinen, 2010; Seidl et al., 2023; Zhai et al., 2023), which uses the cosine similarity between the whole-protein representation \mathbf{p} and

the corresponding part of the small molecule embeddings \mathbf{m}_p , and the activity labels \mathbf{y}_m :

$$\begin{aligned} \mathcal{L}_{\text{LB}}(\mathbf{p}, \{\mathbf{m}_p^m\}_{m=1}^M, \{\mathbf{y}_m\}_{m=1}^M) \\ = -\frac{1}{M} \sum_{m=1}^M \left[\mathbf{y}_m \log(q_m) + (1 - \mathbf{y}_m) \log(1 - q_m) \right], \end{aligned} \quad (14)$$

where $\mathbf{y}_m \in \{0, 1\}$ denotes the activity label for the protein-ligand pair and $q_m = \sigma(s(\mathbf{p}, \mathbf{m}_p^m))$, with the sigmoid function σ .

4. Experiments and Results

We evaluate ConGLUDe on four drug discovery tasks: virtual screening (Section 4.1), target fishing (Section 4.2), binding pocket prediction (Section 4.3), and ligand-conditioned pocket selection (Section 4.4). For each task, we train a separate model with task-specific data splits to ensure that the corresponding test data are excluded from training. We compare against established benchmarks for virtual screening and binding site prediction, and propose new evaluation protocols for target fishing and pocket selection tasks, which lack standardized benchmarks, by assessing the relevant baseline methods ourselves.

Details on the train and test datasets, training procedures, and task-specific evaluation metrics are provided in Sections C, D, and E, respectively.

4.1. Virtual Screening

We compare ConGLUDe against several contrastive learning-based approaches on two established virtual screening benchmarks, DUD-E (Mysinger et al., 2012) and LIT-PCBA (Tran-Nguyen et al., 2020). The baseline methods fall into two categories. First, models with Uni-Mol-based encoders (Zhou et al., 2023; Gao et al., 2024; Han et al., 2025; He et al., 2025; Feng et al., 2025; Wang et al., 2025) rely on explicit pocket representations and require the binding pocket as input. Second, pocket-agnostic methods do not assume prior pocket information. This group includes SPRINT (McNutt et al., 2024), which encodes the entire protein, as well as two hybrid approaches implemented by us that combine DrugCLIP with a pocket predictor, either P2Rank (Krivák & Hoksza, 2018) or VN-EGNN (Sestak et al., 2025). For these hybrids, the top-ranked pocket predicted by the respective method is selected and encoded using DrugCLIP. Results for AUROC, BEDROC, and enrichment factor at 1% are reported in Table 1. Additional results for EF at 0.5% and 5%, as well as comparisons to classical docking and deep learning based methods, are provided in Tables F1 and F2.

On the DUD-E dataset, methods that use the known binding pocket as input significantly outperform approaches, including ConGLUDe, that do not assume pocket informa-

Table 1. Zero-shot virtual screening performance on the DUD-E and LIT-PCBA datasets measured by AUROC, BEDROC, and EF at 1%. For ConGLUDe, we report the median and mean absolute deviation (MAD) over three training re-runs. The best value per column as well as all other values within one MAD are marked in bold.

		DUD-E			LIT-PCBA		
		AUROC \uparrow	BEDROC \uparrow	EF 1% \uparrow	AUROC \uparrow	BEDROC \uparrow	EF 1% \uparrow
†	DrugCLIP (Gao et al., 2024)	80.93	50.52	31.89	57.17	6.23	5.51
†	DrugHash (Han et al., 2025)	83.73	57.16	37.18	54.58	7.14	6.14
†	S ² Drug (He et al., 2025)	92.46	79.25	43.06	58.23	8.69	7.38
†	LigUnity (Feng et al., 2025)	89.22	65.26	42.63	59.85	11.33	6.47
†	HypSeek (Wang et al., 2025)	94.35	78.92	51.44	62.10	11.96	6.81
	DrugCLIP _{P2Rank} ^a	58.29	7.45	3.75	49.72	2.96	2.44
	DrugCLIP _{VN-EGNN} ^a	69.24	28.18	17.02	52.52	3.56	2.58
	SPRINT (McNutt et al., 2024)	69.01 ^a	13.26 ^a	4.85 ^a	73.40	12.30	10.78
	ConGLUDe	81.29 ± 1.11	49.49 ± 1.94	31.76 ± 1.13	64.06 ± 3.25	12.24 ± 2.06	11.03 ± 1.81

† Known binding pocket given as input.

^a Evaluated in this work.

tion. However, when the binding pocket is unknown, which is common in many virtual screening settings, DrugCLIP would need to rely on predicted pockets. In this scenario, its performance drops substantially and becomes markedly worse than that of ConGLUDe. Notably, the other natively pocket agnostic method, SPRINT, also performs significantly worse than ConGLUDe on DUD-E. On the more realistic LIT-PCBA benchmark, natively pocket-agnostic approaches significantly outperform pocket-requiring methods, even when the correct pocket is provided as input to the latter. Overall, ConGLUDe is the only model that demonstrates strong cross-benchmark generalization.

4.2. Zero-Shot Target Fishing

Target fishing refers to the task of identifying protein targets for a given small molecule ligand. We evaluate ConGLUDe on a target fishing dataset from Reinecke et al. (2024), which contains experimentally determined targets for approximately 1,000 ligands. These targets were identified using Kinobeads chemical proteomics, an experimental technology that differs substantially from the data sources used to train ConGLUDe. As a result, this dataset represents a challenging out-of-domain setting, which we address in a zero-shot manner.

In Table 2, we compare ConGLUDe to DrugCLIP (Gao et al., 2024), SPRINT (McNutt et al., 2024), and DiffDock (Corso et al., 2023). Since DrugCLIP requires pocket structures, which are unavailable for this dataset, we generate candidate pockets using P2Rank and VN-EGNN. ConGLUDe consistently outperforms all baselines, and the difference in per-ligand AUCs between ConGLUDe and DiffDock is highly significant (Wilcoxon test, $p \approx 10^{-24}$). All other methods perform close to random, highlighting the challenge of the task, while DiffDock’s evaluation requires multiple GPU-days, making it impractical for large-scale virtual

screening or target fishing.

Table 2. Zero-shot performance on the target fishing task measured by mean AUROC, Δ AUPRC, and EF at 1% with standard deviations across small molecules. The best value per column is marked in bold. ConGLUDe significantly outperforms the second best method ((Wilcoxon test, $p \approx 10^{-24}$)).

	AUROC \uparrow	Δ AUPRC \uparrow	EF 1% \uparrow
DrugCLIP _{P2Rank}	51.2 ± 17.5	0.6 ± 2.1	1.4 ± 6.4
DrugCLIP _{VN-EGNN}	54.2 ± 20.1	0.4 ± 1.3	0.8 ± 7.6
SPRINT	42.5 ± 14.3	0.3 ± 1.2	0.8 ± 3.3
DiffDock	58.9 ± 17.7	2.2 ± 4.5	5.3 ± 14.1
ConGLUDe	65.6 ± 20.4	5.1 ± 10.2	9.9 ± 19.4

4.3. Binding Site Prediction

As shown in Table 3, we retain the performance of VN-EGNN on binding site prediction which highlights the robustness of the VN-EGNN encoder. The architectural modifications and adaptations to support additional tasks do not hinder its ability to perform well on pocket prediction. Full results of compared methods from Sestak et al. (2025) are in Appendix Table F3.

Table 3. Performance at binding site identification measured by the top-1 DCC success rate at a 4Å threshold (\uparrow) on the COACH420, HOLO4K, and PDBbind datasets. Best value marked bold.

	COACH420	HOLO4K	PDBBind2020
VN-EGNN	0.605	0.532	0.669
ConGLUDe	0.602	0.525	0.689

4.4. Ligand-Conditioned Pocket Selection

Finally, we evaluate *ligand-conditioned pocket selection*, where candidate pockets are ranked by their likelihood of

binding a given ligand, in contrast to unconditioned predictors that ignore ligand information. We compare against two unconditioned baselines, P2Rank (Krivák & Hoksza, 2018) and VN-EGNN (Sestak et al., 2025), as well as two-step approaches that pair DrugCLIP (Gao et al., 2024) with an unconditioned pocket predictor, ranking pockets by similarity between DrugCLIP-encoded pocket and ligand representations. We further include DiffDock (Corso et al., 2023), a blind docking method that implicitly selects binding pockets during docking. Unlike docking, which explicitly simulates each ligand–pocket pair, ConGLUDe embeds ligands and pockets independently and scores them via a dot product, resulting in a substantial speed advantage.

We evaluated on a PDBbind time split (Stärk et al., 2022) and the allosteric site database (ASD) (Liu et al., 2020), reporting top-1 DCC success rate at 4 Å. ConGLUDe outperforms all baselines on PDBbind (Table 4). On ASD, performance drops for all methods due to allosteric pockets that are rarely seen during training, and unconditioned predictors frequently miss these sites. ConGLUDe, unlike DrugCLIP still improves ligand-specific selection over unconditioned baselines, but overall accuracy is limited by VN-EGNN’s detection of allosteric pockets. Details are discussed in Appendix Section F.3.

Table 4. Performance of ligand-conditioned pocket selection measured by the top-1 DCC success rate at a 4 Å threshold (\uparrow). Values in parentheses indicate 95% confidence intervals obtained by bootstrapping. The best-performing method is highlighted in bold.

	PDBbind Time	ASD
P2Rank	0.45 ^(.41, .50)	0.24 ^(.23, .26)
VN-EGNN	0.39 ^(.34, .43)	0.20 ^(.18, .21)
DrugCLIP _{P2Rank}	0.42 ^(.37, .47)	0.24 ^(.22, .26)
DrugCLIP _{VN-EGNN}	0.41 ^(.36, .45)	0.19 ^(.18, .21)
DiffDock	0.37 ^(.33, .42)	0.33 ^(.31, .35)
ConGLUDe	0.47 ^(.43, .52)	0.29 ^(.27, .30)

4.5. Ablation Studies

We performed an ablation study on the main components of ConGLUDe: a) structure-based training data, b) ligand-based training data, c) geometric loss, d) contrastive loss between molecule and protein, and e) contrastive loss between molecule and binding site. The results of the ablation study are shown in Table 5. On LIT-PCBA, ablating each component leads to a deterioration of the performance metrics, which indicates that all components together contribute to the effectiveness of ConGLUDe. On the DUD-E benchmark, structure-based data are critical for performance, while ligand-based data are not strictly necessary and, in fact, removing them even slightly improves results, albeit at the cost of reduced generalizability to more realistic datasets such as LIT-PCBA. Ablating individual loss terms, that are not directly responsible for virtual screening, has little effect on virtual screening performance. Nevertheless, all components are essential for enabling the learning of other tasks, including pocket prediction ($\mathcal{L}_{\text{geometric}}$), target fishing (\mathcal{L}_{m2p}), and pocket selection (\mathcal{L}_{m2b}).

5. Conclusion

We present ConGLUDe, a contrastive learning-based method for drug discovery, which enables the unified training on structure- and ligand-based data by integrating a geometric binding site prediction module directly within the protein encoder. With this approach, ConGLUDe achieves state-of-the-art performance across a variety of both traditionally structure- and ligand-based tasks with high computational efficiency, demonstrating its broad applicability.

Limitations. While ConGLUDe performs well for proteins with experimentally resolved 3D structures as found in the PDB, its behavior on predicted structures or proteins highly divergent from known templates remains uncertain. Moreover, its extension to ligand-based data currently assumes bioassays with a uniquely associated protein target and does not directly support phenotypic or target-agnostic assays. Although ConGLUDe can identify ligand-specific

Table 5. Ablation study: Performance on virtual screening on the DUD-E (Mysinger et al., 2012) and LIT-PCBA (Tran-Nguyen et al., 2020) datasets measured by AUROC, BEDROC and EF at 1%. ConGLUDe results are reported from a single run using the same random seed as the ablated models.

	DUD-E			LIT-PCBA		
	AUROC \uparrow	BEDROC \uparrow	EF 1% \uparrow	AUROC \uparrow	BEDROC \uparrow	EF 1% \uparrow
only SB data	83.88	56.20	36.57	53.06	5.48	4.73
only LB data	67.11	10.61	5.31	67.94	11.11	9.38
no $\mathcal{L}_{\text{geometric}}$	83.26	53.05	34.79	64.17	11.41	10.06
no \mathcal{L}_{m2p}	82.58	50.30	32.26	64.80	11.01	10.24
no \mathcal{L}_{m2b}	81.55	50.16	32.34	64.90	10.97	8.98
ConGLUDe	82.04	50.80	32.52	66.25	13.63	12.25

pockets substantially faster than traditional docking or co-folding approaches, it does not generate docked ligand conformations. For applications that require explicit docking, ConGLUDe-predicted pockets can nevertheless serve as an efficient starting point for standard docking workflows.

Outlook. Despite its already strong performance across diverse tasks, ConGLUDe could be extended in several promising directions. Integrating generative models could enable joint prediction and design of ligands for specific pockets. The framework could also be extended to the prediction of additional properties such as binding affinity or ADMET profiles. More generally, our approach suggests a path toward general-purpose foundation models for drug discovery that jointly learn from structural protein-ligand complexes and large-scale bioactivity data.

Software and Data

The code for ConGLUDe is available at <https://github.com/ml-jku/conglude>.

Acknowledgements

The ELLIS Unit Linz, the LIT AI Lab, the Institute for Machine Learning, are supported by the Federal State Upper Austria. We thank the projects FWF AIRI FG 9-N (10.55776/FG9), AI4GreenHeatingGrids (FFG- 899943), Stars4Waters (HORIZON-CL6-2021-CLIMATE-01-01), FWF Bilateral Artificial Intelligence (10.55776/COE12). We thank Merck Healthcare KGaA, NXAI GmbH, Audi AG, Silicon Austria Labs (SAL), GLS (Univ. Waterloo), TÜV Holding GmbH, Software Competence Center Hagenberg GmbH, dSPACE GmbH, TRUMPF SE + Co. KG.

References

Abramson, J., Adler, J., Dunger, J., Evans, R., Green, T., Pritzel, A., Ronneberger, O., Willmore, L., Ballard, A. J., Bambrick, J., et al. Accurate structure prediction of biomolecular interactions with alphafold 3. *Nature*, pp. 1–3, 2024. [1](#)

Babajide Mustapha, I. and Saeed, F. Bioactive molecule prediction using extreme gradient boosting. *Molecules*, 21(8):983, 2016. [2](#)

Ballester, P. J. and Mitchell, J. B. O. A machine learning approach to predicting protein-ligand binding affinity with applications to molecular docking. *Bioinformatics*, 26(9): 1169–1175, 2010. [19](#)

Berman, H. M., Westbrook, J., Feng, Z., Gilliland, G., Bhat, T. N., Weissig, H., Shindyalov, I. N., and Bourne, P. E. The protein data bank. *Nucleic Acids Research*, 28(1): 235–242, 2000. [1](#)

Beveridge, D. L. and Dicapua, F. M. Free energy via molecular simulation: applications to chemical and biomolecular systems. *Annual review of biophysics and biophysical chemistry*, 18(1):431–492, 1989. [1](#)

Bongers, B. J., IJzerman, A. P., and Van Westen, G. J. P. Proteochemometrics – recent developments in bioactivity and selectivity modeling. *Drug Discovery Today: Technologies*, 32-33:89–98, 2019. [2](#)

Brocidacono, M., Francoeur, P., Aggarwal, R., Popov, K. I., Koes, D. R., and Tropsha, A. BigBind: Learning from Nonstructural Data for Structure-Based Virtual Screening. *Journal of Chemical Information and Modeling*, 64(7): 2488–2495, 2024. [2](#), [19](#)

Burbridge, R., Trotter, M., Buxton, B., and Holden, S. Drug design by machine learning: support vector machines for pharmaceutical data analysis. *Computers & chemistry*, 26(1):5–14, 2001. [2](#)

Corso, G., Stärk, H., Jing, B., Barzilay, R., and Jaakkola, T. Diffdock: Diffusion steps, twists, and turns for molecular docking. In *International Conference on Learning Representations (ICLR)*, 2023. [1](#), [7](#), [8](#), [16](#)

Cournia, Z., Chipot, C., Roux, B., York, D. M., and Sherman, W. Free energy methods in drug discovery—introduction. In *Free Energy Methods in Drug Discovery: Current State and Future Directions*, pp. 1–38. 2021. [1](#)

De Vivo, M., Masetti, M., Bottegoni, G., and Cavalli, A. Role of molecular dynamics and related methods in drug discovery. *Journal of Medicinal Chemistry*, 59(9):4035–4061, 2016. [1](#)

Discovery, C., Boitreaud, J., Dent, J., McPartlon, M., Meier, J., Reis, V., Rogozhnikov, A., and Wu, K. Chai-1: Decoding the molecular interactions of life. *bioRxiv*, pp. 2024–10, 2024. [1](#)

Du, X., Li, Y., Xia, Y.-L., Ai, S.-M., Liang, J., Sang, P., Ji, X.-L., and Liu, S.-Q. Insights into protein–ligand interactions: mechanisms, models, and methods. *International Journal of Molecular Sciences*, 17(2):144, 2016. [1](#)

Durrant, J. D. and McCammon, J. A. NNScore 2.0: a neural-network receptor-ligand scoring function. *Journal of Chemical Information and Modeling*, 51(11):2897–2903, 2011. doi: 10.1021/ci2003889. [19](#)

Ester, M., Kriegel, H.-P., Sander, J., and Xu, X. A density-based algorithm for discovering clusters in large spatial databases with noise. In *International Conference on Knowledge Discovery and Data Mining*, pp. 226–231, 1996. [5](#)

Fan, J., Fu, A., and Zhang, L. Progress in molecular docking. *Quantitative Biology*, 7:83–89, 2019. [1](#)

Feng, B., Liu, Z., Li, H., Yang, M., Zou, J., Cao, H., Li, Y., Zhang, L., and Wang, S. Hierarchical affinity landscape navigation through learning a shared pocket-ligand space. *Patterns*, 6(10):101371, 2025. [2](#), [6](#), [7](#), [20](#)

Francoeur, P. G., Masuda, T., Sunseri, J., Jia, A., Iovanisci, R. B., Snyder, I., and Koes, D. R. Three-dimensional convolutional neural networks and a cross-docked data set for structure-based drug design. *Journal of Chemical Information and Modeling*, 60(9):4200–4215, 2020. [2](#)

Fürst, A., Rumetshofer, E., Lehner, J., Tran, V. T., Tang, F., Ramsauer, H., Kreil, D., Kopp, M., Klambauer, G., Bitto, A., et al. Cloob: Modern hopfield networks with infoloob outperform clip. In *Advances in Neural Information Processing Systems (NeurIPS)*, 2022. [6](#)

Gao, B., Qiang, B., Tan, H., Jia, Y., Ren, M., Lu, M., Liu, J., Ma, W.-Y., and Lan, Y. DrugCLIP: Contrastive Protein-Molecule Representation Learning for Virtual Screening. In *Advances in Neural Information Processing Systems (NeurIPS)*, 2024. [2](#), [3](#), [6](#), [7](#), [8](#), [16](#), [20](#)

Gaulton, A., Bellis, L. J., Bento, A. P., Chambers, J., Davies, M., Hersey, A., Light, Y., McGlinchey, S., Michalovich, D., Al-Lazikani, B., and Overington, J. P. ChEMBL: a large-scale bioactivity database for drug discovery. *Nucleic Acids Research*, 40(D1):D1100–D1107, 2011. [2](#), [5](#), [16](#)

Gil-Sorribes, M., Serrano, A. C., and Molina, A. Tensor-DTI: Enhancing biomolecular interaction prediction with contrastive embedding learning. In *Learning Meaningful Representations of Life (LMRL) Workshop at ICLR 2025*, 2025. [3](#)

Gilson, M. K., Liu, T., Baitaluk, M., Nicola, G., Hwang, L., and Chong, J. BindingDB in 2015: A public database for medicinal chemistry, computational chemistry and systems pharmacology. *Nucleic Acids Research*, 44(D1):D1045–D1053, 2015. [5](#), [16](#)

Gohlke, H., Hendlich, M., and Klebe, G. Knowledge-based scoring function to predict protein-ligand interactions. *Journal of Molecular Biology*, 295(2):337–356, 2000. [1](#)

Gutmann, M. and Hyvärinen, A. Noise-contrastive estimation: A new estimation principle for unnormalized statistical models. In *International conference on artificial intelligence and statistics*, pp. 297–304, 2010. [6](#)

Halgren, T. A., Murphy, R. B., Friesner, R. A., Beard, H. S., Frye, L. L., Pollard, W. T., and Banks, J. L. Glide: a new approach for rapid, accurate docking and scoring. 2. Enrichment factors in database screening. *Journal of Medicinal Chemistry*, 47(7):1750–1759, 2004. [19](#)

Han, J., Hong, Y., and Li, W.-J. DrugHash: Hashing Based Contrastive Learning for Virtual Screening. *Proceedings of the AAAI Conference on Artificial Intelligence*, 39(16):17041–17049, 2025. [2](#), [3](#), [6](#), [7](#), [20](#)

Hansch, C., Maloney, P. P., Fujita, T., and Muir, R. M. Correlation of biological activity of phenoxyacetic acids with hammett substituent constants and partition coefficients. *Nature*, 194(4824):178–180, 1962. [2](#)

He, B., Gao, B., Chen, Y., Lan, Y., Ma, C., Yu, P. S., Zhang, Y.-Q., and Ma, W.-Y. S²drug: Bridging protein sequence and 3d structure in contrastive representation learning for virtual screening, 2025. [2](#), [6](#), [7](#), [20](#)

Jia, Y., Gao, B., Tan, J., Zheng, J., Hong, X., Zhu, W., Tan, H., Xiao, Y., Tan, L., Cai, H., Huang, Y., Deng, Z., Wu, X., Jin, Y., Yuan, Y., Tian, J., He, W., Ma, W., Zhang, Y., Liu, L., Yan, C., Zhang, W., and Lan, Y. Deep contrastive learning enables genome-wide virtual screening. *Science*, 391(6781), 2026. [2](#)

Jumper, J., Evans, R., Pritzel, A., Green, T., Figurnov, M., Ronneberger, O., Tunyasuvunakool, K., Bates, R., Žídek, A., Potapenko, A., Bridgland, A., Meyer, C., Kohl, S. A. A., Ballard, A. J., Cowie, A., Romera-Paredes, B., Nikolov, S., Jain, R., Adler, J., Back, T., Petersen, S., Reiman, D., Clancy, E., Zielinski, M., Steinegger, M., Pacholska, M., Berghammer, T., Bodenstein, S., Silver, D., Vinyals, O., Senior, A. W., Kavukcuoglu, K., Kohli, P., and Hassabis, D. Highly accurate protein structure prediction with AlphaFold. *Nature*, 596(7873):583–589, 2021. [2](#), [16](#)

Kim, S., Chen, J., Cheng, T., Gindulyte, A., He, J., He, S., Li, Q., Shoemaker, B., Thiessen, P., Yu, B., Zaslavsky, L., Zhang, J., and Bolton, E. Pubchem 2025 update. *Nucleic Acids Research*, 53(D1):D1516–D1525, 2024. [2](#), [5](#), [16](#)

Kinch, M. S., Kraft, Z., and Schwartz, T. 2023 in review: FDA approvals of new medicines. *Drug Discovery Today*, pp. 103966, 2024. [1](#)

Krivák, R. and Hoksza, D. P2Rank: machine learning based tool for rapid and accurate prediction of ligand binding sites from protein structure. *Journal of Cheminformatics*, 10(1):1–12, 2018. [6](#), [8](#), [17](#)

Kuntz, I. D., Blaney, J. M., Oatley, S. J., Langridge, R., and Ferrin, T. E. A geometric approach to macromolecule-ligand interactions. *Journal of Molecular Biology*, 161(2):269–288, 1982. [1](#)

Landrum, G. and contributors, R. Rdkit: Open-source cheminformatics software, 2006. URL <https://www.rdkit.org>. [3](#), [17](#)

Lapinsh, M., Prusis, P., Gutcaits, A., Lundstedt, T., and Wikberg, J. E. Development of proteo-chemometrics: a novel technology for the analysis of drug-receptor interactions. *Biochimica et Biophysica Acta (BBA) - General Subjects*, 1525:180–190, 2001. [2](#)

Lenselink, E. B., Ten Dijke, N., Bongers, B., Papadatos, G., Van Vlijmen, H. W., Kowalczyk, W., IJzerman, A. P., and Van Westen, G. J. Beyond the hype: deep neural networks outperform established methods using a ChEMBL bioactivity benchmark set. *Journal of cheminformatics*, 9:1–14, 2017. [2](#)

Lin, Z., Akin, H., Rao, R., Hie, B., Zhu, Z., Lu, W., Smetanin, N., Verkuil, R., Kabeli, O., Shmueli, Y., et al. Evolutionary-scale prediction of atomic-level protein structure with a language model. *Science*, 379(6637): 1123–1130, 2023. [3](#) [17](#)

Liu, L., Zhang, S., He, D., Ye, X., Zhou, J., Zhang, X., Jiang, Y., Diao, W., Yin, H., Chai, H., Wang, F., He, J., Zheng, L., Li, Y., and Fang, X. Pre-Training on Large-Scale Generated Docking Conformations with HelixDock to Unlock the Potential of Protein-ligand Structure Prediction Models, 2024. [2](#)

Liu, X., Lu, S., Song, K., Shen, Q., Ni, D., Li, Q., He, X., Zhang, H., Wang, Q., Chen, Y., et al. Unraveling allosteric landscapes of allosterome with ASD. *Nucleic Acids Research*, 48(D1), 2020. [8](#) [17](#)

Loshchilov, I. and Hutter, F. Decoupled Weight Decay Regularization. In *International Conference on Learning Representations*, 2019. [19](#)

Luukkonen, S., Meijer, E., Tricarico, G. A., Hofmans, J., Stouten, P. F. W., van Westen, G. J. P., and Lenselink, E. B. Large-Scale Modeling of Sparse Protein Kinase Activity Data. *Journal of Chemical Information and Modeling*, 63 (12):3688–3696, 2023. [5](#)

Macalino, S. J. Y., Gosu, V., Hong, S., and Choi, S. Role of computer-aided drug design in modern drug discovery. *Archives of pharmacal research*, 38:1686–1701, 2015. [1](#)

Mayr, A., Klambauer, G., Unterthiner, T., Steijaert, M., Wegner, J. K., Ceulemans, H., Clevert, D.-A., and Hochreiter, S. Large-scale comparison of machine learning methods for drug target prediction on chembl. *Chemical science*, 9(24):5441–5451, 2018. [2](#)

McNutt, A. T., Francoeur, P., Aggarwal, R., Masuda, T., Meli, R., Ragoza, M., Sunseri, J., and Koes, D. R. GNINA 1.0: molecular docking with deep learning. *Journal of Cheminformatics*, 13(1):43, 2021. [19](#)

McNutt, A. T., Adduri, A. K., Ellington, C. N., Dayao, M. T., Xing, E. P., Mohimani, H., and Koes, D. R. SPRINT Enables Interpretable and Ultra-Fast Virtual Screening against Thousands of Proteomes. *arXiv preprint arXiv:2411.15418*, 2024. [2](#) [3](#) [5](#) [6](#) [7](#) [16](#) [20](#)

Merz Jr, K. M., Ringe, D., and Reynolds, C. H. *Drug design: structure-and ligand-based approaches*. Cambridge University Press, 2010. [2](#)

Morgan, H. L. The Generation of a Unique Machine Description for Chemical Structures—A Technique Developed at Chemical Abstracts Service. *Journal of Chemical Documentation*, 5(2):107–113, 1965. [3](#)

Muratov, E. N., Bajorath, J., Sheridan, R. P., Tetko, I. V., Filimonov, D., Poroikov, V., Oprea, T. I., Baskin, I. I., Varnek, A., Roitberg, A., et al. QSAR without borders. *Chemical Society Reviews*, 49(11):3525–3564, 2020. [2](#)

Mutharasappan, N., Ravi Rao, G., Mariadasse, R., Poopandi, S., Mathimaran, A., Dhamodharan, P., Sundarraj, R., Jeyaraj Pandian, C., and Jeyaraman, J. Experimental and computational methods to determine protein structure and stability. *Frontiers in Protein Structure, Function, and Dynamics*, pp. 23–55, 2020. [1](#)

Mysinger, M. M., Carchia, M., Irwin, J. J., and Shoichet, B. K. Directory of Useful Decoys, Enhanced (DUD-E): Better Ligands and Decoys for Better Benchmarking. *Journal of Medicinal Chemistry*, 55(14):6582–6594, 2012. [6](#) [8](#) [17](#)

Passaro, S., Corso, G., Wohlwend, J., Reveiz, M., Thaler, S., Somnath, V. R., Getz, N., Portnoi, T., Roy, J., Stark, H., Kwabi-Addo, D., Beaini, D., Jaakkola, T., and Barzilay, R. Boltz-2: Towards Accurate and Efficient Binding Affinity Prediction. *bioRxiv*, 2025. [2](#)

Pei, Q., Gao, K., Wu, L., Zhu, J., Xia, Y., Xie, S., Qin, T., He, K., Liu, T.-Y., and Yan, R. Fabind: Fast and accurate protein-ligand binding, 2024. [1](#)

Praski, M., Adamczyk, J., and Czech, W. Benchmarking Pretrained Molecular Embedding Models For Molecular Representation Learning, 2025. *arXiv:2508.06199 [cs]*. [5](#)

Radford, A., Kim, J. W., Hallacy, C., Ramesh, A., Goh, G., Agarwal, S., Sastry, G., Askell, A., Mishkin, P., Clark, J., Krueger, G., and Sutskever, I. Learning transferable visual models from natural language supervision. In *International Conference on Machine Learning*, volume 139, 2021. [6](#)

Reinecke, M., Brear, P., Vornholz, L., Berger, B.-T., Seefried, F., Wilhelm, S., Samaras, P., Gyenis, L., Litchfield, D. W., Médard, G., et al. Chemical proteomics

reveals the target landscape of 1,000 kinase inhibitors. *Nature Chemical Biology*, 20(5):577–585, 2024. 7, 17

Rogers, D. and Hahn, M. Extended-connectivity fingerprints. *Journal of Chemical Information and Modeling*, 50:742–754, 5 2010. 17

Sanchez-Fernandez, A., Rumetshofer, E., Hochreiter, S., and Klambauer, G. Cloome: contrastive learning unlocks bioimaging databases for queries with chemical structures. *Nature Communications* 2023 14:1, 14:1–14, 11 2023. 6

Satorras, V. G., Hoogeboom, E., and Welling, M. E(n) Equivariant Graph Neural Networks. In *International Conference on Machine Learning*, 2021. 15

Schimunek, J., Seidl, P., Friedrich, L., Kuhn, D., Rippmann, F., Hochreiter, S., and Klambauer, G. Context-enriched molecule representations improve few-shot drug discovery. *arXiv preprint arXiv:2305.09481*, 2023. 2

Seidl, P., Vall, A., Hochreiter, S., and Klambauer, G. Enhancing activity prediction models in drug discovery with the ability to understand human language. *Proceedings of Machine Learning Research*, 202:30458–30490, 3 2023. 2, 5, 6

Sestak, F., Schneckenreiter, L., Brandstetter, J., Hochreiter, S., Mayr, A., and Klambauer, G. VN-EGNN: E(3)- and SE(3)-Equivariant Graph Neural Networks with Virtual Nodes Enhance Protein Binding Site Identification. *J Cheminform*, 2025. 3, 4, 5, 6, 7, 8, 15, 16, 17, 20

Sheridan, R. P., Wang, W. M., Liaw, A., Ma, J., and Gifford, E. M. Extreme Gradient Boosting as a Method for Quantitative Structure–Activity Relationships. *Journal of Chemical Information and Modeling*, 56(12):2353–2360, 2016. 2

Siemers, F. M., Feldmann, C., and Bajorath, J. Minimal data requirements for accurate compound activity prediction using machine learning methods of different complexity. *Cell Reports Physical Science*, 0(0), 2022. 5

Singh, R., Sledzieski, S., Bryson, B., Cowen, L., and Berger, B. Contrastive learning in protein language space predicts interactions between drugs and protein targets. *Proceedings of the National Academy of Sciences*, 120(24): e2220778120, 2023. 2, 3

Spitzer, R. and Jain, A. N. Surfflex-Dock: Docking benchmarks and real-world application. *Journal of Computer-Aided Molecular Design*, 26(6):687–699, 2012. 19

Stärk, H., Ganea, O., Pattanaik, L., Barzilay, R., and Jaakkola, T. EquiBind: Geometric Deep Learning for Drug Binding Structure Prediction. In *International Conference on Machine Learning*, 2022. 1, 8, 17

Steinegger, M. and Söding, J. MMseqs2 enables sensitive protein sequence searching for the analysis of massive data sets. *Nature Biotechnology*, 35(11):1026–1028, 2017. 16

Stepniewska-Dziubinska, M., Zielenkiewicz, P., and Siedlecki, P. Pafnucy – A deep neural network for structure-based drug discovery. 12 2017. 19

Svensson, E., Hoedt, P.-J., Hochreiter, S., and Klambauer, G. Hyperpcm: Robust task-conditioned modeling of drug–target interactions. *Journal of Chemical Information and Modeling*, 64(7):2539–2553, 2024. 2

Svetnik, V., Liaw, A., Tong, C., Culberson, J. C., Sheridan, R. P., and Feuston, B. P. Random forest: a classification and regression tool for compound classification and qsar modeling. *Journal of chemical information and computer sciences*, 43(6):1947–1958, 2003. 2

Tran-Nguyen, V.-K., Jacquemard, C., and Rognan, D. LIT-PCBA: An Unbiased Data Set for Machine Learning and Virtual Screening. *Journal of Chemical Information and Modeling*, 60(9):4263–4273, 2020. 6, 8, 17

Trott, O. and Olson, A. J. AutoDock Vina: improving the speed and accuracy of docking with a new scoring function, efficient optimization, and multithreading. *Journal of Computational Chemistry*, 31(2), 2010. 19

Truchon, J.-F. and Bayly, C. I. Evaluating virtual screening methods: good and bad metrics for the "early recognition" problem. *Journal of Chemical Information and Modeling*, 47(2):488–508, 2007. 19

Unterthiner, T., Mayr, A., Klambauer, G., Steijaert, M., Wegner, J. K., Ceulemans, H., and Hochreiter, S. Deep learning as an opportunity in virtual screening. In *Proceedings of the Deep Learning Workshop at NIPS*, volume 27, pp. 1–9, 2014. 5

Vella, D. and Ebejer, J.-P. Few-shot learning for low-data drug discovery. *Journal of chemical information and modeling*, 63(1):27–42, 2022. 2

Vemula, D., Jayasurya, P., Sushmitha, V., Kumar, Y. N., and Bhandari, V. Cadd, ai and ml in drug discovery: A comprehensive review. *European Journal of Pharmaceutical Sciences*, 181:106324, 2023. 1

Wang, J., Zhu, W., Gao, B., Hong, X., Zhang, Y.-Q., Ma, W.-Y., and Lan, Y. Learning Protein-Ligand Binding in Hyperbolic Space, 2025. 2, 6, 7, 20

Wang, R., Fang, X., Lu, Y., Yang, C.-Y., and Wang, S. The PDBbind database: methodologies and updates. *Journal of Medicinal Chemistry*, 48(12):4111–4119, 2005. 5, 16, 17

Wang, Z., Wang, Z., Yang, M., Pang, L., Nie, F., Liu, S., Gao, Z., Zhao, G., Ji, X., Huang, D., et al. Enhancing challenging target screening via multimodal protein-ligand contrastive learning. *bioRxiv*, 2024. [3](#)

Wohlwend, J., Corso, G., Passaro, S., Reveiz, M., Leidal, K., Swiderski, W., Portnoi, T., Chinn, I., Siltterra, J., Jaakkola, T., et al. Boltz-1: Democratizing biomolecular interaction modeling. *bioRxiv*, 2024. [1](#)

Yang, K., Swanson, K., Jin, W., Coley, C., Eiden, P., Gao, H., Guzman-Perez, A., Hopper, T., Kelley, B., Mathea, M., et al. Analyzing learned molecular representations for property prediction. *Journal of chemical information and modeling*, 59(8):3370–3388, 2019. [2](#)

Zhai, X., Mustafa, B., Kolesnikov, A., and Beyer, L. Sigmoid loss for language image pre-training. In *Proceedings of the IEEE/CVF international conference on computer vision*, pp. 11975–11986, 2023. [6](#)

Zhang, X., Gao, H., Wang, H., Chen, Z., Zhang, Z., Chen, X., Li, Y., Qi, Y., and Wang, R. PLANET: A Multi-objective Graph Neural Network Model for Protein-Ligand Binding Affinity Prediction. *Journal of Chemical Information and Modeling*, 64(7):2205–2220, 2024. [19](#)

Zheng, L., Fan, J., and Mu, Y. OnionNet: a Multiple-Layer Intermolecular-Contact-Based Convolutional Neural Network for Protein-Ligand Binding Affinity Prediction. *ACS Omega*, 4(14):15956–15965, 2019. [19](#)

Zhou, G., Gao, Z., Ding, Q., Zheng, H., Xu, H., Wei, Z., Zhang, L., and Ke, G. Uni-Mol: A Universal 3D Molecular Representation Learning Framework. In *International Conference on Learning Representations*, 2023. [6](#)

Öztürk, H., Özgür, A., and Ozkirimli, E. DeepDTA: deep drug–target binding affinity prediction. *Bioinformatics*, 34(17):i821–i829, 2018. [2](#)

A. Notation

The following table summarizes all notation used throughout this paper.

Definition	Symbol	Type
Scalars		
batch size	J	\mathbb{N}
contrastive space dimension	D	\mathbb{N}
VN-EGNN output dimension	E	\mathbb{N}
number of binding site VNs	N	\mathbb{N}
number of predicted binding sites after clustering	K	\mathbb{N}
number of labeled small molecules for a given protein	M	\mathbb{N}
number of protein residues	S	\mathbb{N}
Representations		
protein residue representation	\mathbf{h}'_s	\mathbb{R}^E
pocket representation before clustering	\mathbf{b}'_n	\mathbb{R}^E
protein representation before projection	\mathbf{p}'	\mathbb{R}^E
pocket representation before projection	$\hat{\mathbf{b}}_k$	\mathbb{R}^E
final protein representation	\mathbf{p}	\mathbb{R}^D
final pocket representation	\mathbf{b}_k	\mathbb{R}^D
small molecule representation	$\mathbf{m}_m = [\mathbf{m}_{\text{pm}}, \mathbf{m}_{\text{bm}}]$	\mathbb{R}^{2D}
Coordinates		
protein residue position	\mathbf{x}'_s	\mathbb{R}^3
pocket node position before clustering	\mathbf{z}'_k	\mathbb{R}^3
predicted binding pocket center/final VN position	$\hat{\mathbf{z}}_n$	\mathbb{R}^3
Data quantities		
predicted confidence value for $\hat{\mathbf{z}}_n$	\hat{c}_n	\mathbb{R}
ground-truth confidence value for $\hat{\mathbf{z}}_n$	c_n	$\{c_0, [0.5, 1]\}$
residue-level binding site label	z_s	$\{0, 1\}$
binary activity label for molecule \mathbf{m}_m	y_m	$\{0, 1\}$
Constants		
fall-back value for confidence calculation	c_0	0.001
tolerance radius for confidence calculation	γ	4.0
temperature for \mathcal{L}_{p2m}	τ_{p2m}	$\frac{1}{\sqrt{2D}}$
temperature for \mathcal{L}_{m2p}	τ_{m2p}	$\frac{1}{\sqrt{D}}$
temperature for \mathcal{L}_{m2b}	τ_{m2b}	$\frac{1}{\sqrt{D}}$
Functions		
cosine similarity	$s(\cdot, \cdot)$	$\mathbb{R}^D \times \mathbb{R}^D \rightarrow [-1, 1]$
sigmoid function	$\sigma(\cdot, \cdot)$	$\mathbb{R} \rightarrow [0, 1]$

The InfoNCE loss used for structure-based training is defined as follows:

$$\text{InfoNCE}(\mathbf{q}^j, \mathbf{k}^j, \{\mathbf{k}^i\}_{i=1}^J; \tau) = -\log \frac{\exp(s(\mathbf{q}^j, \mathbf{k}^j)/\tau)}{\sum_{i=1}^J \exp(s(\mathbf{q}^j, \mathbf{k}^i)/\tau)}. \quad (\text{A.1})$$

B. VN-EGNN Details

B.1. Heterogeneous Message Passing

Following [Sestak et al. \(2025\)](#), we briefly summarize the heterogeneous message passing scheme used in VN-EGNN. Each layer consists of three message passing steps that exchange information between protein residues (\mathcal{R}) and virtual binding pocket nodes (\mathcal{B}).

The first step corresponds to the standard equivariant graph neural network (EGNN) formulation ([Satorras et al., 2021](#)), where information is exchanged between neighboring protein residues:

Message passing step 1 ($\mathcal{R} \rightarrow \mathcal{R}$):

$$\boldsymbol{\mu}_{ij}^{(\mathcal{R}\mathcal{R})} = \phi_{e^{(\mathcal{R}\mathcal{R})}}(\mathbf{h}_i, \mathbf{h}_j, \|\mathbf{x}_i - \mathbf{x}_j\|) \quad (\text{B.1})$$

$$\boldsymbol{\mu}_i^{(\mathcal{R}\mathcal{R})} = \frac{1}{|\mathcal{N}(i)|} \sum_{j \in \mathcal{N}(i)} \boldsymbol{\mu}_{ij}^{(\mathcal{R}\mathcal{R})} \quad (\text{B.2})$$

$$\mathbf{x}_i = \mathbf{x}_i + \frac{1}{|\mathcal{N}(i)|} \sum_{j \in \mathcal{N}(i)} \frac{\mathbf{x}_i - \mathbf{x}_j}{\|\mathbf{x}_i - \mathbf{x}_j\|} \phi_{\mathbf{x}^{(\mathcal{R}\mathcal{R})}}(\boldsymbol{\mu}_{ij}^{(\mathcal{R}\mathcal{R})}) \quad (\text{B.3})$$

$$\mathbf{h}_i = \mathbf{h}_i + \phi_{h^{(\mathcal{R}\mathcal{R})}}(\mathbf{h}_i, \boldsymbol{\mu}_i^{(\mathcal{R}\mathcal{R})}). \quad (\text{B.4})$$

Here, the coordinates \mathbf{x}_i and features \mathbf{h}_i of residue nodes are updated based on aggregated messages from their neighbors. The MLPs $\phi_{e^{(\mathcal{R}\mathcal{R})}}$, $\phi_{\mathbf{x}^{(\mathcal{R}\mathcal{R})}}$, and $\phi_{h^{(\mathcal{R}\mathcal{R})}}$ are learnable functions specific to each layer. The same applies to all MLPs ϕ in the subsequent steps.

In the second step, residue nodes transmit information to virtual pocket nodes \mathcal{B} , which act as proxies for potential binding sites:

Message passing step 2 ($\mathcal{R} \rightarrow \mathcal{B}$):

$$\boldsymbol{\mu}_{ij}^{(\mathcal{R}\mathcal{B})} = \phi_{e^{(\mathcal{R}\mathcal{B})}}(\mathbf{b}_i, \mathbf{h}_j, \|\mathbf{z}_i - \mathbf{x}_j\|) \quad (\text{B.5})$$

$$\boldsymbol{\mu}_i^{(\mathcal{R}\mathcal{B})} = \frac{1}{S} \sum_{j=1}^S \boldsymbol{\mu}_{ij}^{(\mathcal{R}\mathcal{B})} \quad (\text{B.6})$$

$$\mathbf{z}_i = \mathbf{z}_i + \frac{1}{S} \sum_{j=1}^S \frac{\mathbf{z}_i - \mathbf{x}_j}{\|\mathbf{z}_i - \mathbf{x}_j\|} \phi_{\mathbf{x}^{(\mathcal{R}\mathcal{B})}}(\boldsymbol{\mu}_{ij}^{(\mathcal{R}\mathcal{B})}) \quad (\text{B.7})$$

$$\mathbf{b}_i = \mathbf{b}_i + \phi_{h^{(\mathcal{R}\mathcal{B})}}(\mathbf{b}_i, \boldsymbol{\mu}_i^{(\mathcal{R}\mathcal{B})}) \quad (\text{B.8})$$

Finally, the third step propagates information in the reverse direction, from virtual nodes back to residue nodes:

Message passing step 3 ($\mathcal{B} \rightarrow \mathcal{R}$):

$$\boldsymbol{\mu}_{ij}^{(\mathcal{B}\mathcal{R})} = \phi_{e^{(\mathcal{B}\mathcal{R})}}(\mathbf{h}_i, \mathbf{b}_j, \|\mathbf{x}_i - \mathbf{z}_j\|) \quad (\text{B.9})$$

$$\boldsymbol{\mu}_i^{(\mathcal{B}\mathcal{R})} = \frac{1}{N} \sum_{j=1}^N \boldsymbol{\mu}_{ij}^{(\mathcal{B}\mathcal{R})} \quad (\text{B.10})$$

$$\mathbf{x}_i = \mathbf{x}_i + \frac{1}{N} \sum_{j=1}^N \frac{\mathbf{x}_i - \mathbf{z}_j}{\|\mathbf{x}_i - \mathbf{z}_j\|} \phi_{\mathbf{x}^{(\mathcal{B}\mathcal{R})}}(\boldsymbol{\mu}_{ij}^{(\mathcal{B}\mathcal{R})}) \quad (\text{B.11})$$

$$\mathbf{h}_i = \mathbf{h}_i + \phi_{h^{(\mathcal{B}\mathcal{R})}}(\mathbf{h}_i, \boldsymbol{\mu}_i^{(\mathcal{B}\mathcal{R})}) \quad (\text{B.12})$$

B.2. Objective Functions

VN-EGNN ([Sestak et al., 2025](#)) is trained using a combination of losses that supervise the prediction of binding site centers, residue-level segmentation, and confidence of the predictions.

To ensure accurate prediction of the binding site center (bsc) location, the squared distance between the true binding site center \mathbf{z} and the closest predicted center $\hat{\mathbf{z}}_n$ among N candidates is minimized:

$$\mathcal{L}_{\text{bsc}}(\{\hat{\mathbf{z}}_1, \dots, \hat{\mathbf{z}}_N\}, \mathbf{z}) = \min_{n \in 1, \dots, N} \|\mathbf{z} - \hat{\mathbf{z}}_n\|^2. \quad (\text{B.13})$$

For residue-level binding site segmentation, the network outputs predictions for each residue s through a multilayer perceptron: $\hat{z}_s = \text{MLP}(\mathbf{h}'_s)$. The segmentation loss is defined as a differentiable Dice loss, which compares the predicted and true residue labels z_s :

$$\mathcal{L}_{\text{seg}}(\{\hat{z}_1, \dots, \hat{z}_S\}, \{z_1, \dots, z_S\}; \epsilon) = 1 - \frac{2 \sum_{s=1}^S z_s \hat{z}_s + \epsilon}{\sum_{n=1}^N z_s + \sum_{n=s}^S \hat{z}_s + \epsilon}, \quad (\text{B.14})$$

where ϵ is a small constant to stabilize the division.

Moreover, each predicted center $\hat{\mathbf{z}}_n$ is assigned a confidence score \hat{c}_n which should reflect its proximity to the true center. The target confidence c_n is defined as:

$$c_n = \begin{cases} 1 - \frac{1}{2\gamma} \cdot \|\mathbf{z} - \hat{\mathbf{z}}_n\| & \text{if } \|\mathbf{z} - \hat{\mathbf{z}}_n\| \leq \gamma, \\ c_0 & \text{otherwise,} \end{cases}, \quad (\text{B.15})$$

and the corresponding confidence loss is the mean squared error between predicted and target confidences:

$$\mathcal{L}_{\text{confidence}}(\{\hat{c}_1, \dots, \hat{c}_N\}, \{c_1, \dots, c_N\}) = \frac{1}{N} \sum_{n=1}^N (c_n - \hat{c}_n)^2. \quad (\text{B.16})$$

The total VNEGNN objective combines the three components and is used as the geometric learning objective in ConGLUDe's structure-based training:

$$\mathcal{L}_{\text{geometric}} = \mathcal{L}_{\text{bsc}} + \mathcal{L}_{\text{seg}} + \mathcal{L}_{\text{confidence}}. \quad (\text{B.17})$$

C. Datasets

C.1. Structure-Based Training Datasets

For structure-based training, we utilized subsets of PDBbind v.2020 (Wang et al., 2005), adopting the dataset partitions established by the baseline methods corresponding to each task. Specifically, for virtual screening and target fishing, we followed the DrugCLIP split (Gao et al., 2024). For binding site prediction, we trained on scPDB, consistent with VN-EGNN (Sestak et al., 2025), and for ligand-conditioned pocket selection, we employed the time-based split used in DiffDock (Corso et al., 2023).

C.2. Ligand-Based Training Datasets

For the training on the ligand-based data, we employed the MERGED dataset introduced in SPRINT (McNutt et al., 2024), which integrates data from PubChem (Kim et al., 2024), BindingDB (Gilson et al., 2015), and ChEMBL (Gaulton et al., 2011). We use the combined MERGED training and test splits as the basis for our training set and keep the same validation split as (McNutt et al., 2024). For each protein in the dataset, we used an available 3D structure from the PDB; if none was available, we generated an AlphaFold2 (Jumper et al., 2021) structure. To prevent information leakage, proteins with more than 90% sequence identity to any test protein were excluded, using MMSeqs2 (Steinegger & Söding, 2017) with a coverage threshold of 0.8. The number of unique proteins and total data points for each task subset can be found in Table C1.

Table C1. Number of PLI data points in structure-based (SB) and ligand-based (LB) training and validation datasets.

Task	SB Data			LB Data		
	Train Complexes	Val Complexes	Proteins	Train Data Points	Proteins	Val Data Points
Virtual Screening	24,896	400	3,526	56,187,278	47	5,809,414
Pocket Prediction	14,564	1,610	3,103	49,493,389	44	5,539,515
Pocket Selection	24,127	1,384	3,685	57,096,449	45	5,523,271

C.3. Test Datasets

We evaluated our models on diverse benchmark datasets tailored to each task.

For virtual screening, we used two widely adopted benchmarks, DUD-E (Mysinger et al., 2012) and LIT-PCBA (Tran-Nguyen et al., 2020). The DUD-E dataset contains 22,886 active compounds against 102 protein targets, paired with property-matched decoys designed to mimic physical characteristics of active molecules while differing in topology. LIT-PCBA complements DUD-E by providing experimentally validated high-throughput screening results across 15 targets. Unlike DUD-E, which uses synthetic decoys, LIT-PCBA relies exclusively on assay data, resulting in a more realistic and more challenging benchmark for large-scale virtual screening.

Pocket prediction performance was evaluated on three established datasets, which were also used in Sestak et al. (2025). Coach420 (Krivák & Hoksza, 2018) is a curated benchmark of 420 proteins with annotated binding sites on single-chain structures. HOLO4K (Krivák & Hoksza, 2018) consists of over 4,000 holo protein structures with experimentally verified binding pockets, many of which are large multi-chain complexes. For both, Coach420 and HOLO4K, we adopt the so-called *mlig* subsets, as detailed in Krivák & Hoksza (2018), which encompass only biologically relevant ligands. Finally, the PDBbind v.2020 refined set (Wang et al., 2005) includes high-quality protein-ligand complexes with reliable structural and binding affinity data, serving as a stringent benchmark for pocket localization in realistic docking scenarios.

For ligand-conditioned pocket selection, we employed the temporal test split of PDBbind introduced in EquiBind (Stärk et al., 2022), which ensures temporal separation between training and evaluation complexes, thereby simulating prospective prediction performance. In addition, we constructed a new benchmark based on the Allosteric Site Database (ASD, June 2023 release) (Liu et al., 2020). This dataset comprises protein–ligand complexes annotated with allosteric binding sites, providing a novel and challenging testbed for evaluating the generalization of models beyond orthosteric binding interactions. We filtered out all proteins overlapping with the PDBbind training and validation sets proteins.

For target fishing, we use the Kinobeads chemical proteomics dataset of Reinecke et al. (2024). The study profiled 1,183 kinase-directed small molecules in cancer-cell lysates by competitive enrichment on immobilized inhibitors, reports apparent affinities (K_d^{app}) from a two-dose competition design (100 nM and 1 μ M) and provides high-confidence target calls via a trained random-forest classifier. We treat these calls as positives and use the remaining measured proteins as negatives when ranking targets per compound. The raw data are publicly available via ProteomicsDB. After pre-processing and mapping gene symbols to the PDB structure with the highest resolution among those annotated for *Homo sapiens* (if available), we obtained a dataset of 985 ligands and 2,714 proteins.

Table C2 summarizes the number of data points, unique proteins and unique ligands for each test dataset. Figure C1 shows the distribution of maximum ECFP Tanimoto similarities between each test molecule and all training molecules.

D. Hyperparameters and Training Details

For the protein encoder, we adopt VN-EGNN with the default parameters reported by Sestak et al. (2025), i.e., a 5-layer architecture with distinct weights per layer, input dimension 1280 (from ESM-2 embeddings (Lin et al., 2023)), output dimension 100, SiLU activation, and residual connections. Two linear projection layers are trained to map binding site and protein nodes into the contrastive space of dimension $D = 256$.

Ligands are represented as extended connectivity fingerprints (Rogers & Hahn, 2010) with radius 2 and length 2048, concatenated with a vector of 210 chemical descriptors from RdKit (Landrum & contributors, 2006), yielding an input dimension of 2258. The ligand encoder is a two-layer MLP with hidden dimension 512, output dimension $2D = 512$,

Table C2. Summary of test datasets used for evaluation across different tasks. LB = ligand-based datasets, SB = structure-based datasets.

Dataset	Type	Data Points	Unique Proteins	Unique Ligands
DUD-E	LB	1,434,019	102	1,200,431
LIT-PCBA	LB	2,808,770	15 (129)	383,772
Coach420	SB	348	300	278
HOLO4K	SB	4235	3,446	1,700
PDBbind Refined	SB	5,309	5,309	4,482
ASD	SB	1802	1765	1117
PDBbind Time	SB	384	321	328
Kinobeads	LB	1,424,686	2,714	985

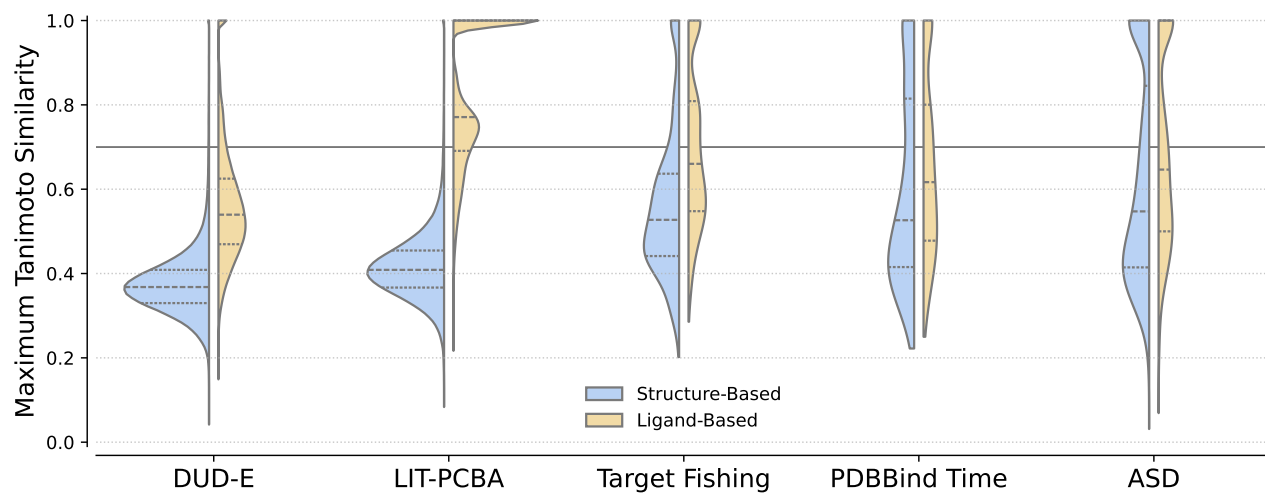


Figure C1. Distributions of maximum Tanimoto similarities between ECFP count fingerprints (radius 2, length 2048) of test-set molecules and those in the structure- and ligand-based training sets.

GELU activation, 10% input dropout, and 50% dropout on the hidden layer.

Training uses a batch size of 64 on structure-based data, resulting in 63 negative ligands per protein and vice versa through in-batch negative sampling. For ligand-based training, each batch contains 16 proteins, with actives and inactives sampled at a 1:3 ratio and capped at 10,000 active ligands per protein. Contrastive loss temperature parameters are set to the inverse square root of the respective embedding dimensions, i.e., $\tau_{p2m} = \frac{1}{\sqrt{2D}}$ and $\tau_{m2p} = \tau_{m2b} = \frac{1}{\sqrt{D}}$. All loss terms are weighted equally in structure-based training, while the ligand-based loss is scaled by a factor of 6 to match the magnitude of L_{SB} .

We optimize using AdamW (Loshchilov & Hutter, 2019) with an initial learning rate of 10^{-3} . A learning rate scheduler reduces the rate by a factor of 10 when the validation metric does not improve for 30 epochs, with a minimum learning rate of 10^{-6} . Early stopping with a patience of 100 epochs is applied based on the same validation metric. Separate models were trained for each task due to the different data splits and training was conducted on NVIDIA A100 GPUs with 40GB memory for 200–350 epochs.

E. Metrics

Depending on the task, we employ different evaluation metrics, which are described below.

For virtual screening, we evaluate the area under the receiver operating characteristic curve (AUROC), the Boltzmann-enhanced discrimination of ROC (BEDROC) at $\alpha = 85$, and enrichment factors (EF) at the top 0.5%, 1% and 5%.

Unlike AUROC, which treats all parts of the ranking equally and is therefore a strong general-purpose metric, BEDROC is tailored to virtual screening scenarios where early recognition of actives is critical (Truchon & Bayly, 2007). The EF at top $x\%$ quantifies the over-representation of actives among the highest-ranked molecules. An EF of 1 corresponds to random ranking, while larger values indicate stronger enrichment.

For target fishing, we evaluate Δ AUPRC, which measures the improvement in area under the precision–recall curve relative to a random baseline, in addition to AUROC and EF at 1%,

For binding pocket prediction, we measure the DCC (distance from predicted pocket center to ground-truth pocket center) or DCA (distance from predicted pocket center to the closest atom of the corresponding ligand) success rates at 4 Å. For a protein with k ground-truth pockets, we consider the k top-ranked binding sites. The success rate is the fraction of ground-truth pockets where at least one predicted pocket satisfies the DCC or DCA threshold of 4 Å.

For ligand-conditioned pocket selection, we consider the DCC success rate at 4 Å of the top-ranked predicted pocket compared to all ground-truth pockets associated with the given ligand.

F. Extended Results

F.1. Virtual Screening

Tables F1 and F2 show the complete evaluation on DUD-E and LIT-PCBA split by dataset. We compare against a diverse set of representative baselines, detailed below, spanning classical docking engines, pose-aware machine learning models, and modern contrastive learning methods.

Classical docking engines such as Glide-SP (Halgren et al., 2004), AutoDock Vina (Trott & Olson, 2010), and Surflex (Spitzer & Jain, 2012) explicitly sample ligand conformations within predefined binding pockets and rank poses using empirical or physics-inspired scoring functions. Pose-based machine learning methods, including NN-Score (Durrant & McCammon, 2011), RF-Score (Ballester & Mitchell, 2010), and Gnina (McNutt et al., 2021), operate on docked complexes and leverage learned scoring functions to predict binding affinity or pose quality.

Deep learning models that require explicit pocket definitions are also included in the comparison. These comprise voxel-based 3D CNNs such as Pafnucy (Stepniewska-Dziubinska et al., 2017), distance-based representations such as OnionNet (Zheng et al., 2019), and graph neural network approaches including BigBind (Brocidiaco et al., 2024) and PLANET (Zhang et al., 2024). These methods directly exploit geometric and chemical features of the binding site and are typically applied as docking rescoring or refinement tools.

More recent contrastive and embedding-based approaches aim to bypass explicit docking by learning joint representations of

proteins and ligands. DrugCLIP (Gao et al., 2024), DrugHash (Han et al., 2025), S²Drug (He et al., 2025), LigUnity (Feng et al., 2025), and HypSeek (Wang et al., 2025) align ligand embeddings with structure-based pocket or protein representations, enabling fast similarity-based virtual screening. In contrast, SPRINT (McNutt et al., 2024) adopts a ligand-based formulation using whole-protein representations, which supports broad target coverage but does not allow pocket-specific predictions.

Table F1. Zero-shot virtual screening performance on the LIT-PCBA datasets measured by AUROC, BEDROC, and EF at 0.5%, 1% and 5%. For ConGLUDe, we report the median and mean absolute deviation (MAD) over three training re-runs. The best value per column as well as all other values within one MAD are marked in bold.

	AUROC (%)	BEDROC (%)	0.5%	EF	
				1%	5%
Surflex	51.47	-	-	2.50	-
Glide-SP	53.15	4.00	3.17	3.41	2.01
Planet	57.31	-	4.64	3.87	2.43
GninA	60.93	5.40	-	4.63	-
DeepDTA	56.27	2.53	-	1.47	-
BigBind	60.80	-	-	3.82	-
DrugCLIP	57.17	6.23	8.56	5.51	2.27
DrugHash	54.58	7.14	9.65	6.14	2.42
S ² Drug	58.23	8.69	11.44	7.38	2.97
LigUnity	59.85	11.33	-	6.47	-
HypSeek	62.10	11.96	-	6.81	-
DrugCLIP _{P2Rank}	49.72	2.96	2.41	2.44	1.36
DrugCLIP _{VN-EGNN}	52.52	3.56	1.82	2.58	1.59
SPRINT	73.40	12.30	15.90	10.78	5.29
ConGLUDe	64.06 ± 3.25	12.24 ± 2.06	15.87 ± 2.03	11.03 ± 1.81	4.68 ± 0.30

To visualize the learned representation space, we applied t-SNE to project both protein and ligand embeddings into two dimensions. As shown by one example in Figure F1, active ligands around the embedding of their target protein, whereas inactive ligands are distributed more diffusely across the space. This pattern highlights the model’s ability to capture meaningful protein–ligand relationships.

F.2. Binding Site Prediction

Table F3 reports binding site identification results for all methods compared in Sestak et al. (2025).

F.3. Ligand-conditioned pocket selection

During *ligand-conditioned pocket selection*, methods have to rank binding pockets by their likelihood to bind the a given ligand. Unlike unconditioned pocket predictors that do not have a query ligand as input, our task explicitly conditions on ligand identity and thus supports ligand-specific pocket selection. This is task can also be performed by *blind docking methods*. Our model embeds the ligand and each candidate pocket and scores their compatibility with a single dot product, which makes inference extremely fast. With precomputed pocket representations, thousands of ligands can be encoded in seconds and scored via dot products. In contrast, docking-based baselines must dock every ligand into every candidate pocket, which is orders of magnitude slower.

Table F2. Zero-shot virtual screening performance on the DUD-E datasets measured by AUROC, BEDROC, and EF at 0.5%, 1% and 5%. For ConGLUDe, we report the median and mean absolute deviation (MAD) over three training re-runs. The best value per column as well as all other values within one MAD are marked in bold.

	AUROC (%)	BEDROC (%)	0.5%	EF 1%	5%
Glide-SP	76.70	40.70	19.39	16.18	7.23
Vina	71.60	-	9.13	7.32	4.44
NN-score	68.30	12.20	4.16	4.02	3.12
RFscore	65.21	12.41	4.90	4.52	2.98
Pafnucy	63.11	16.50	4.24	3.86	3.76
OnionNet	59.71	8.62	2.84	2.84	2.20
Planet	71.60	-	10.23	8.83	5.40
DrugCLIP	80.93	50.52	38.07	31.89	10.66
DrugHash	83.73	57.16	43.03	37.18	12.07
S ² Drug	92.46	79.25	58.37	43.06	18.82
LigUnity	89.22	65.26	-	42.63	-
HypSeek	94.35	78.92	-	51.44	-
DrugCLIP _{P2Rank}	58.29	7.04	4.02	3.75	2.38
DrugCLIP _{VN-EGNN}	69.24	28.18	20.45	17.02	6.83
ConGLUDe	81.29 \pm 1.11	49.49 \pm 1.94	39.43 \pm 0.97	31.76 \pm 1.13	10.71 \pm 0.26

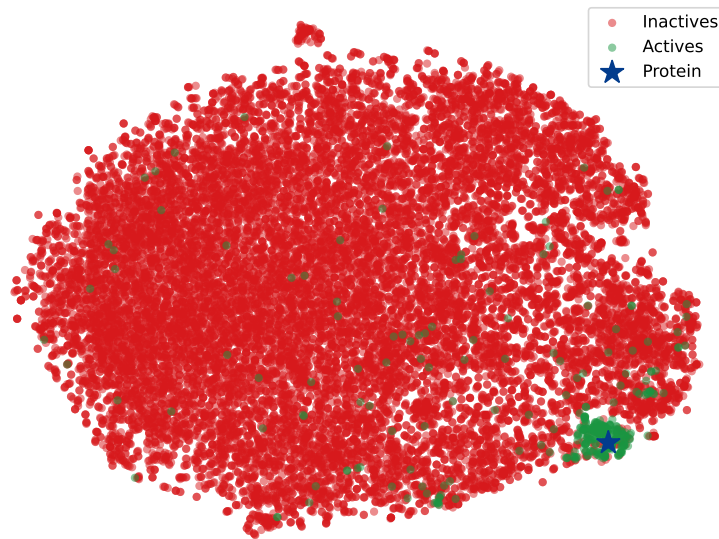


Figure F1. t-SNE projection of protein and ligand embeddings for the DUD-E target with PDB ID 2FSZ.

Table F3. Performance at binding site identification in terms of DCC and DCA success rates at 4 \AA on the COACH420, HOLO4K and PDBbind2020 refined datasets . The best performing method(s) per column are marked bold. The second best in italics.

Methods	COACH420		HOLO4K		PDBbind2020	
	DCC \uparrow	DCA \uparrow	DCC \uparrow	DCA \uparrow	DCC \uparrow	DCA \uparrow
Fpocket	0.228	0.444	0.192	0.457	0.253	0.371
P2Rank	0.464	0.728	0.474	0.787	0.653	0.826
DeepSite	–	0.564	–	0.456	–	–
Kalasanty	0.335	0.636	0.244	0.515	0.416	0.625
DeepSurf	0.386	0.658	0.289	0.635	0.510	0.708
DeepPocket	0.399	0.645	0.456	0.734	0.644	0.813
GAT	0.039	0.130	0.036	0.110	0.032	0.088
GCN	0.049	0.139	0.044	0.174	0.018	0.070
GAT + GCN	0.036	0.131	0.042	0.152	0.022	0.074
GCN2	0.042	0.131	0.051	0.163	0.023	0.089
SchNet	0.168	0.444	0.192	0.501	0.263	0.457
EGNN	0.156	0.361	0.127	0.406	0.143	0.302
EquiPocket	0.423	0.656	0.337	0.662	0.545	0.721
VN-EGNN	0.605	0.750	0.532	0.659	0.669	0.820
ConGLUDe	0.602	0.726	0.525	0.693	0.689	0.856